

Discontinuous Modulation Scheme for a Differential-Mode Ćuk Inverter

Siamak Mehrnami, *Student Member, IEEE*, and Sudip K. Mazumder, *Senior Member, IEEE*

Abstract—The differential-mode Ćuk inverter (DMCI) is a single-stage inverter with low device count. It offers advantages over other topologies because of compactness, higher power density, and reduced cost. It is a promising topological configuration for renewable-/alternative-energy applications with isolated as well as nonisolated structures. The continuous modulation scheme (CMS), which was introduced originally for this inverter, activates all the modules of the DMCI. The new discontinuous modulation scheme (DMS) deactivates one module in each half line-cycle leading to discontinuous operation of modules. This paper outlines the DMS and a mechanism to realize it. The experimental open-loop and closed-loop results of the DMCI using CMS and DMS are provided along with a comparison of their performances. It is shown that, the DMS reduces the circulating power and hence mitigates the losses. The voltage ratings of the devices also are reduced with the DMS. In contrast, the CMS has wider linearity in its normalized dc-voltage gain and yields reduced harmonic distortion of the output voltage. For DMS, to achieve comparable linearity in normalized dc-voltage gain and distortion, harmonic compensation under closed-loop control is a pathway that has been demonstrated.

Index Terms—Ćuk, differential-mode inverter, high-frequency link, modulation, renewable/alternative energy, single-phase, single-stage, switched mode power supply.

I. INTRODUCTION

FOR low-cost inverter applications, ranging from renewable energy to alternative energy to vehicular applications, with need for galvanic isolation, high-frequency-link (HFL) inverters have emerged as a potential front runner [1]–[7]. Such inverter topologies often have a multistage topological architecture to accommodate the high-frequency transformer that may add to system cost, reliability, loss, and power density. Typical transformer-less topologies [8] have a cascaded boost–buck [9] or buck–boost [10] architecture, which may yield common-mode leakage current for some applications [11]. For such applications and others, an isolated HFL inverter topology is a relevant choice. Kim *et al.* [1] introduce a bidirectional multistage HFL topology, while the topologies outlined in [2]–[4] support unidirectional power flow. While several HFL-inverter

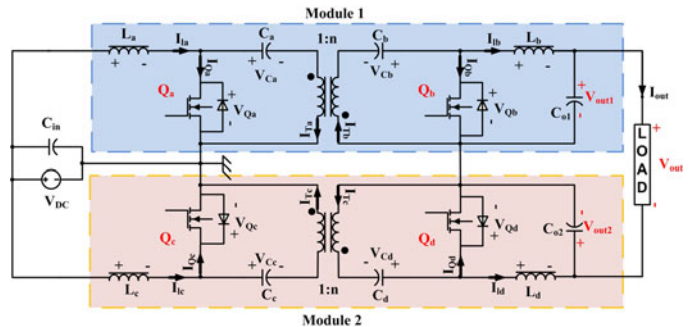


Fig. 1. Illustration of the DMCI topology, which comprises two modules (Modules 1 and 2).

topologies include a front-end dc–dc converter followed by a decoupling dc capacitor [1], other multistage topologies preclude the need for an intermediate dc-link electrolytic capacitor [3], [4]. Overall, for low-power applications the cost-benefit tradeoff of a multistage HFL inverter topology requires careful attention. As such, for low-power single-phase HFL inverter applications, there is an enhanced thrust to seek single-stage topological solutions [12]–[26].

Single-stage topologies are categorized [12], reviewed and compared by literatures [13]–[15]. Long *et al.* [16] present z -source inverter topologies, while [17] introduces Ćuk-derived single-stage topology. Differential inverters are group of single-stage topologies that consist of parallel-series connection of two dc converters. Chen and Wang [18] present differential buck while differential boost is discussed in [19] and [20]. Differential flyback [21], [22] is one of the candidate topologies for microinverters with three controlled devices (with two of them being high-side devices) and three diodes. However, this topology cannot support bidirectional power flow, which will require additional controllable devices. Further current on the secondary side of the bridge is discontinuous in nature. Moreover, the magnetizing current of the isolation transformers is subjected to line-frequency components which affect the size of the transformer. The differential topology introduced by Kjaer and Blaabjerg [23] has the line-frequency penetration on magnetizing current of transformer problem too. Sivasubramanian and Mazumder [24] introduce parallel–parallel isolated configurations with Ćuk converter, but with eight controllable switches.

One topological embodiment for single-stage HFL inverter is the differential-mode Ćuk inverter (DMCI) topology, as shown in Fig. 1, which was originally outlined in [25]. The DMCI topology [26] comprises two modules, which are connected in parallel at the dc side and connected in series at the ac side. The DMCI yields several useful features [12] that directly impact the cost,

Manuscript received August 14, 2013; revised November 22, 2013 and February 9, 2014; accepted March 17, 2014. Date of publication April 1, 2014; date of current version October 15, 2014. Recommended for publication by Associate Editor K.-H. Chen.

The authors are with the Laboratory for Energy and Switching-Electronics Systems, Department of Electrical and Computer Engineering, University of Illinois at Chicago, Chicago, IL 60607 USA (e-mail: smehn2@uic.edu; mazumder@uic.edu).

Color versions of one or more of the figures in this paper are available online at <http://ieeexplore.ieee.org>.

Digital Object Identifier 10.1109/TPEL.2014.2314688

reliability, and power density. The differential-mode inverter comprises limited number of switches all of which are low-side driven. Further, the inverter has the ability to support bidirectional power flow using the same set of switches and a seamless control. Yet another feature of the inverter is its ability to support voltage step-up and step-down functionalities that also enables the utility of the basic differential-mode topology for even nonisolated applications. An added capability of the HFL Ćuk inverter is its ability to support line-frequency ripple current without a large isolation transformer. Due to the presence of the two blocking capacitors on the primary and secondary sides of the transformer, the magnetizing current of the transformer is essentially devoid of any line-frequency current component. Finally, the possibility of coupled inductors and transformer has been introduced in [27], which enhances the compactness of the inverter and leads to reduced input and output ripples.

The original DMCI topology [25] outlined switching of the inverter using a continuous modulation scheme (CMS) [25], [28], in which diagonal devices switch simultaneously and continuously. In CMS, one module pulls the power while the other one pushes it. This leads to circulation of power yielding higher switching and conduction losses. Further, the continuous modulation of all of the switches implies that a control system for this inverter sees an eighth-order dynamics under all operating conditions which has adverse implications on control bandwidth.

This paper outlines a discontinuous modulation scheme (DMS) for the DMCI in Section II along with a description of the CMS. It builds on the abridged work outlined in [28] by the authors. It is noted that, Myrzik [12] suggests the possibility of discontinuous operation of the modules of the DMCI but does not provide any details on either the realization of the modulation or the control scheme. Knight *et al.* [29] outline a discontinuous operation of a six-switch topology that has similarities with the DMCI but the results are not extendable to the DMCI under consideration. Further, either of these two papers does not provide any insight into the performance comparison between DMS and CMS operation of the DMCI. In contrast, in this paper, a detailed analysis on the performance of the DMCI operating with DMS as well as CMS is provided in Sections III and IV based on theoretical and experimental results. These results demonstrate the positive impact of DMS on the DMCI with regard to efficiency and reduction in device breakdown voltage rating while at the same time, requiring relatively complex closed-loop compensation in order to achieve satisfactory total harmonic distortion (THD) and transient response. However, overall cost of the DMS-based DMCI is lower than the CMS-based DMCI because the inverter requires devices with reduced voltage ratings and yields reduced power loss and thermal load. Furthermore, compared to CMS, DMS yields a reduced-order topological control of the DMCI yielding the possibility of an inverter with enhanced stability margin for a suitably designed closed-loop control system.

II. MODULATION SCHEMES FOR THE DMCI

In this section, we first outline the CMS for completeness and then describe the DMS for the DMCI along with the illustrations

for the operating modes and power-flow mechanisms. Overall, while the output power of the DMCI using the DMS and CMS remain continuous, the module power and current using DMS (unlike CMS) is discontinuous; that is, in DMS, each module of the DMCI is activated in alternate half of each line cycle.

A. Continuous Modulation Scheme

The output voltage (V_{out}) of the inverter is the differential of the output voltages (V_{out1} and V_{out2}) of the two dc-dc converter modules. This results in the following normalized dc-voltage gain relationship:

$$\frac{V_{out}}{n \times V_{DC}} = \frac{V_{out1}}{n \times V_{DC}} - \frac{V_{out2}}{n \times V_{DC}} = \left(\frac{D_1}{1 - D_1} - \frac{D_2}{1 - D_2} \right). \quad (1)$$

In (1), V_{DC} is the dc input voltage and n is turns ratio of the transformers. The duty ratios (D_1 and D_2) of Modules 1 and 2 (operating using CMS) are related by $D_1 = 1 - D_2$, so the normalized dc-voltage gain (g) in terms of D_1 is described by the following:

$$g = \frac{V_{out}}{n \times V_{DC}} = \left(\frac{2D_1 - 1}{D_1(1 - D_1)} \right). \quad (2)$$

As will be demonstrated later, depending on n , CMS-based DMCI exhibits relatively linear normalized dc-voltage gain over a finite range of duty cycle.

For CMS, the diagonal switches [i.e., $Q_a(Q_b)$ and $Q_d(Q_c)$] of the two modules are fed with the same gating signals while the two switches [$Q_a(Q_b)$ and $Q_c(Q_d)$] in each of the modules are fed with complementary gating signals. Because the inverter operates in a differential mode, the inductor currents flow from one Ćuk module to the other. There are four modes in all. Modes 1 and 2 are for the positive half of the line cycle while Modes 3 and 4 are for the negative half of the line cycle. Fig. 2 illustrates the four modes of the inverter using CMS.

In Mode 1, switches Q_a and Q_d are turned ON while switches Q_b and Q_c are turned OFF. The current flowing through the input inductor L_a increases and the inductor stores energy. The capacitor C_a discharges through switch Q_a resulting in a transfer of energy from the primary to the secondary side of the top transformer. The energy stored in the capacitor C_b is discharged to the circuit formed by L_b , C_2 , and the load R. During this time interval, the inductor L_d stores energy leading to an increase in its current. The capacitor C_d discharges through switch Q_d . For Module 2, power flows from the secondary to the primary side. The capacitor C_c is discharged to provide the power.

In Mode 2, switches Q_a and Q_d are turned OFF while switches Q_b and Q_c are turned ON. Capacitors C_a and C_d and C_b and C_c are charged using the energy which was stored in the inductors L_a and L_d while switches Q_a and Q_d were ON. During this time interval, inductors L_b and L_c release their stored energy. Finally, Modes 3 and 4 are similar to Modes 1 and 2 with the exception that the load current is negative.

Fig. 3(a) illustrates the realization of the CMS with control loop. The output voltage of the inverter (V_{out}), the output voltage of each module (V_{out1} and V_{out2}), the modulating signal and the duty cycle of Q_a are shown in Fig. 3(b). The output voltages

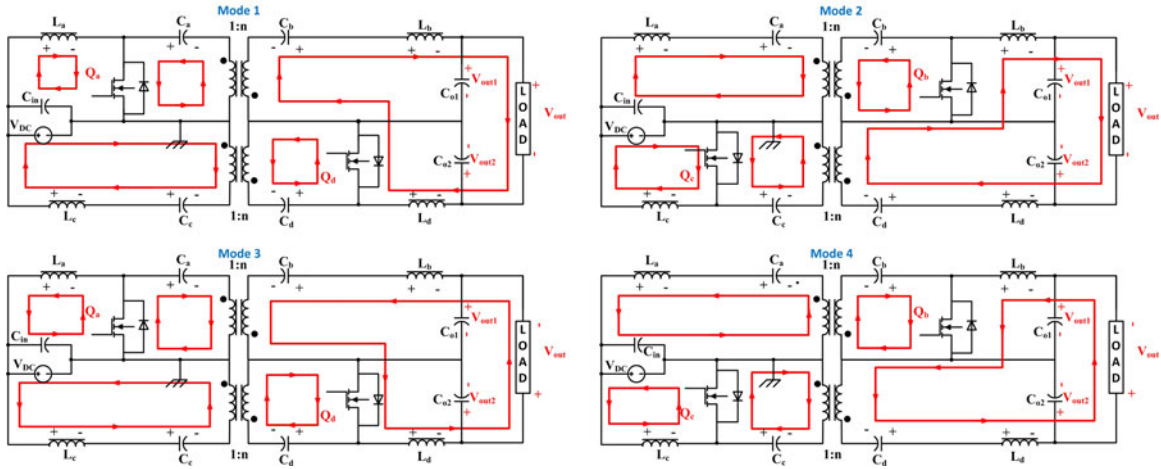


Fig. 2. Modes of operation of the DMCI with CMS.

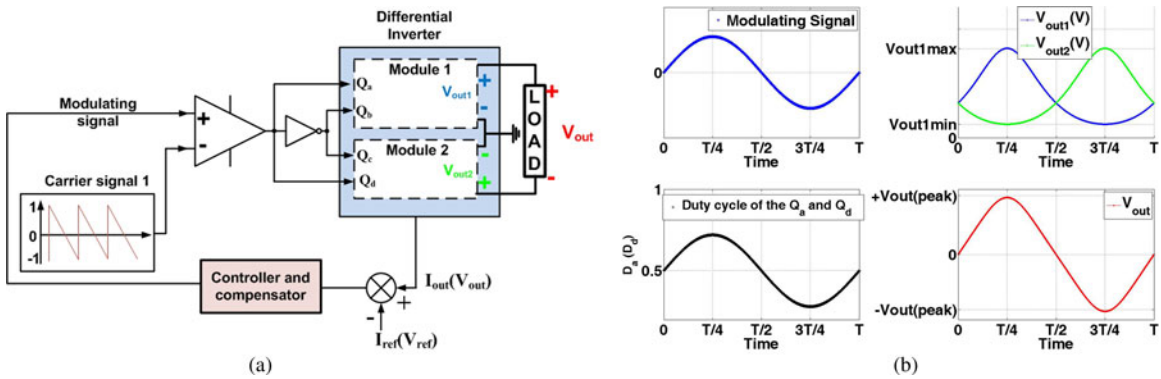


Fig. 3. (a) Illustration of realization of the CMS for the DMCI. (b) Illustration of the modulating signal, duty cycles of the switches Q_a (Q_d), output voltages (V_{out1} and V_{out2}) of Modules 1 and 2, and output voltage (V_{out}) of the DMCI using the CMS.

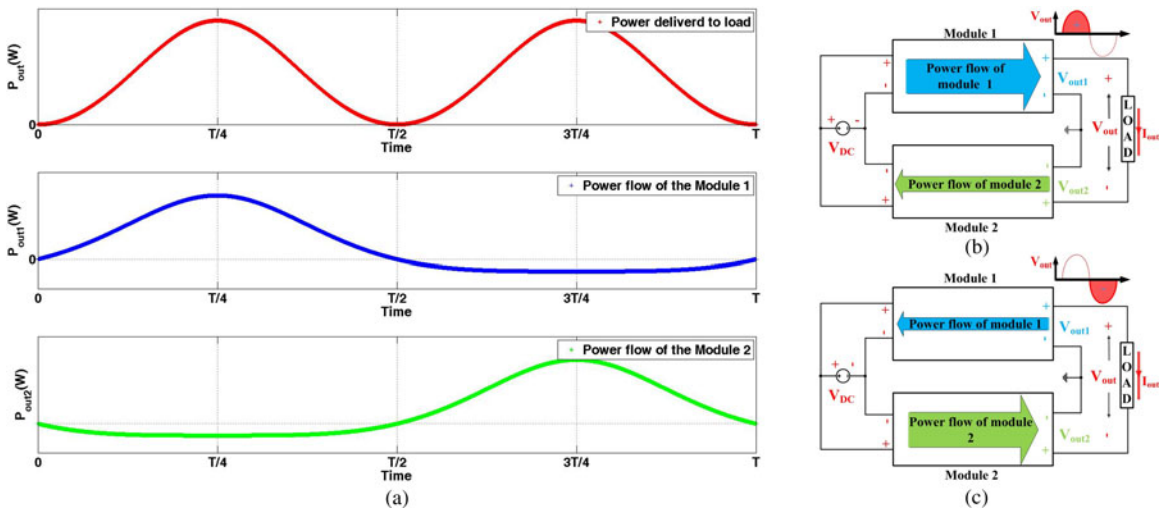


Fig. 4. (a) Instantaneous output powers of the DMCI and its two modules when the DMCI is operated using CMS. (b) and (c) Illustrations of power-flow mechanisms of Modules 1 and 2 during the positive and negative halves of a line cycle.

of both modules are always positive and the minimum voltage depends on amplitude of the modulating signal, with the CMS. The instantaneous power ($p_{out}(t)$) delivered to the load and the instantaneous powers ($p_{out1}(t)$ and $p_{out2}(t)$) flowing through the two modules are shown in Fig. 4(a), assuming a unity power-

factor load. Module 1 delivers positive power from the source to the load in the positive half line cycle, while Module 2 returns part of it from the load to the source. A part of the delivered power returns to the source through Module 1 in the negative half of the line cycle. The power flow diagrams in the positive

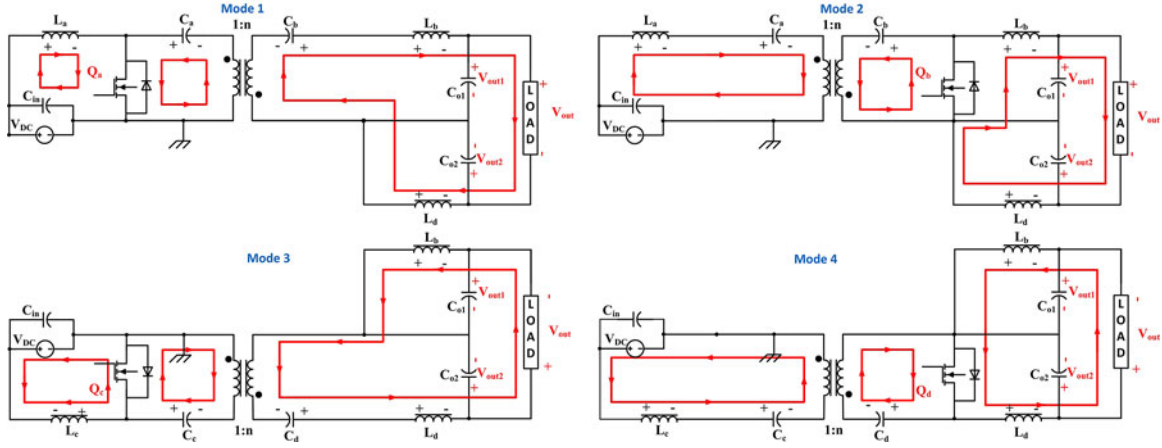


Fig. 5. Modes of operation of the DMCI using DMS.

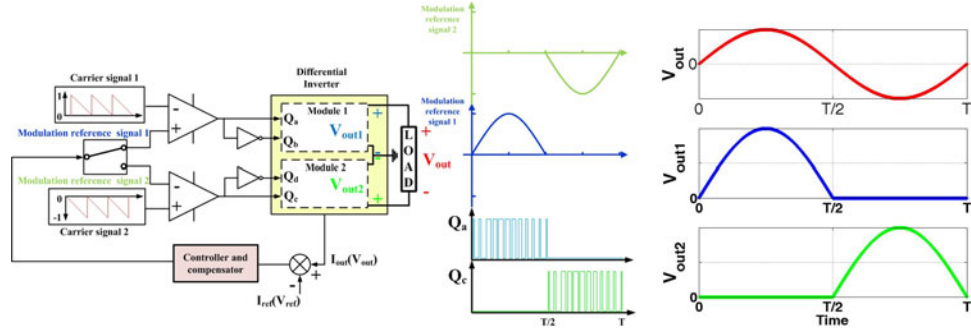


Fig. 6. Illustration of realization of the DMS for the DMCI and the corresponding signals for modulation, switching, and output voltage.

and negative halves of the line cycles are illustrated in Figs. 4(b) and (c), respectively.

B. Discontinuous Modulation Scheme

The CMS was originally introduced for the low-power amplifiers of analog circuits [25] with reduced focus on power loss. For DMCI, and as evident from the illustration in Fig. 4, one of the main drawbacks of the CMS is that it leads to circulating power in the converter yielding extra loss. Moreover, this circulating power also enhances the peak current and peak voltage of the switching devices. Therefore, the main motivation for developing the DMS is to mitigate the circulating power by activating only one of the two modules of the DMCI along with the ac-side switch of the inactive module in negative or positive halves of a line cycle. As such, and as evident in (3), the dc-voltage gain relation of the inverter is dependent in a piecewise manner on D_1 and D_2

$$\begin{aligned} \frac{V_{out}}{n \times V_{DC}} &= \left(\frac{D_1}{1 - D_1} \right) \quad (\text{for } V_{out} > 0) \text{ or} \\ \frac{V_{out}}{n \times V_{DC}} &= \left(\frac{D_2}{1 - D_2} \right) \quad (\text{for } V_{out} < 0). \end{aligned} \quad (3)$$

Fig. 5 shows the modes of operation with DMS. Modes 1 and 2 are for positive half of the line cycle while Modes 3 and 4 are for the negative half of the line cycle. For each of the modes,

a section of the inverter which is inactive is not shown. The capacitor voltage and inductor current in the inactive part of the inverter is zero. Thus, the activation of each of the modules of the DMCI using DMS in alternate half of each line cycle yields a reduction in the order of the inverter by two as compared to the system order obtained using CMS. This is evident in the topological illustrations of the DMCI in Fig. 5 when contrasted with the topological illustration of the DMCI shown in Fig. 2.

Fig. 6 illustrates the closed-loop realization of the DMS-based DMCI. The output voltage (or current) error signal is fed back to the controller, which in turn generates the reference signal for modulation. The modulating signal is bipolar because the output voltage (or current) is bipolar. This signal is fed to the two modules alternately depending on the polarity of the output voltage. Consequently, the resultant modulating reference signals for each module is discontinuous in nature, as illustrated in Fig. 6. As evident in Fig. 6, even though the resultant output voltages (V_{out1} and V_{out2}) of the modules are discontinuous in nature, the differential output voltage (V_{out}) of the DMCI is continuous in form. Assuming a unity-power-factor load (for illustration only), the instantaneous power delivered to the load ($p_{out}(t)$) and the instantaneous power flowing through each of the two modules [$p_{out1}(t)$ and $p_{out2}(t)$] is shown in Fig. 7(a). The flow of power flow in the DMCI in the positive and negative halves of the line cycle are illustrated, respectively, in Figs. 7(b) and (c).

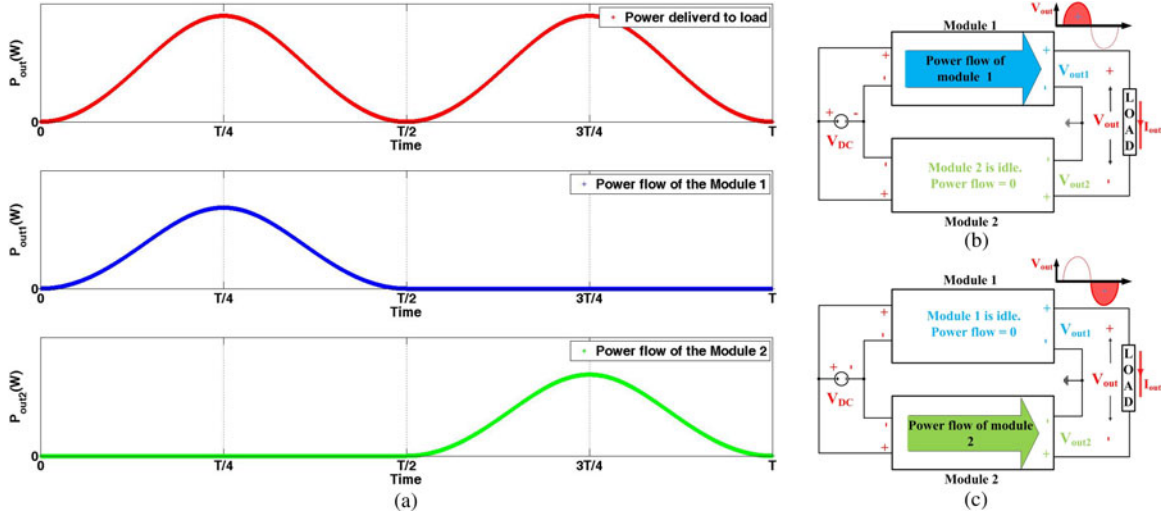


Fig. 7. (a) Instantaneous output power of the DMCI and its individual modules using DMS. (b) and (c) Mechanisms of power flow for the modules of the DMCI during the positive and negative halves of the line cycle.

III. ANALYSIS OF DMS AND CMS

This section provides the theoretical evaluation and analysis of the CMS and the DMS assuming ideal switching condition. In the following section, validating experimental results are provided.

A. Circulating Power

As explained in Section II, there is no circulating power with the DMS operated DMCI. In contrast, the CMS-based DMCI incorporates active as well as circulating reactive power, as illustrated in Fig. 4(a). Using Fryze's definition [30], one can calculate the reactive power of each module of the DMCI. Because both modules have the same power ratings, only one module (i.e., Module 1) is selected here for the calculation of the active and the reactive powers as outlined below

$$P_{out1} = \langle p_{out1}(t) \rangle_{avg} = \frac{1}{T} \int_0^T V_{out1}(t) \times I_{out}(t) dt \quad (4)$$

$$\begin{aligned} S_{out1}^2 &= P_{out1}^2 + Q_{out1}^2 = V_{out1}^2(\text{rms}) \times I_{out1}^2(\text{rms}) \\ &= \frac{1}{T} \int_0^T V_{out1}^2(t) dt \times \frac{1}{T} \int_0^T I_{out1}^2(t) dt. \end{aligned} \quad (5)$$

In (4) and (5), $p_{out1}(t)$ is the instantaneous power, P_{out1} is the active power, Q_{out1} is the circulating reactive power, S_{out1} is the apparent power, and V_{out1} and I_{out} are output voltage and output current of Module 1. Using (4) and (5), the ratio of the reactive to the active power can be derived to be the following:

$$\frac{Q_{out1}}{P_{out1}} = \sqrt{\frac{\frac{1}{T} \int_0^T V_{out1}^2(t) dt \times \frac{1}{T} \int_0^T I_{out1}^2(t) dt}{\left[\frac{1}{T} \int_0^T V_{out1}(t) \times I_{out}(t) dt \right]^2}} - 1. \quad (6)$$

Assuming a unity-power-factor load and negligible THD for the load voltage and the load current, we obtain

$$\begin{cases} I_{out} = I_{out}^* \sin(\omega t) \\ V_{out} = V_{out}^* \sin(\omega t) = nV_{DC} \times g^* \sin(\omega t) \end{cases} \quad (7)$$

where g^* represents the peak normalized dc-voltage gain and is defined to be equal to $\frac{V_{out}^*}{n \times V_{DC}}$. The dc-voltage gains of the DMCI is defined by (2) while the dc-voltage gain of Module 1 (i.e., g_1) is defined by (8) for operation of the DMCI using the CMS

$$g_1 = \frac{V_{out1}}{n \times V_{DC}} = \left(\frac{D_1}{1 - D_1} \right). \quad (8)$$

Using (2) and (8), the relation between g and g_1 is found to be the following:

$$g_1 = \frac{g}{2} + \sqrt{\left(\frac{g}{2} \right)^2 + 1}. \quad (9)$$

Using (8) and (9), V_{out1} is found to be the following:

$$V_{out1} = nV_{DC} \left(\frac{g^* \sin(\omega t)}{2} + \sqrt{\left(\frac{g^* \sin(\omega t)}{2} \right)^2 + 1} \right). \quad (10)$$

Substituting V_{out1} from (10) and I_{out} from (7) into (6) and simplifying the resultant expression yields

$$\begin{aligned} \frac{Q_{out1}}{P_{out1}} &= \frac{\int_0^T \left(\frac{g^* \sin(\omega t)}{2} + \sqrt{\left(\frac{g^* \sin(\omega t)}{2} \right)^2 + 1} \right)^2 dt \times \int_0^T \sin^2(\omega t) dt}{\left[\int_0^T \left(\frac{g^* \sin(\omega t)}{2} + \sqrt{\left(\frac{g^* \sin(\omega t)}{2} \right)^2 + 1} \right) \times \sin(\omega t) dt \right]^2} - 1 \\ &= \frac{\int_0^T \left(\frac{g^{*2} \sin^2(\omega t)}{2} + 1 \right) dt \times \int_0^T \sin^2(\omega t) dt}{\left[\int_0^T \frac{g^*}{2} \sin^2(\omega t) dt \right]^2} - 1 \end{aligned} \quad (11)$$

$$\frac{Q_{out1}}{P_{out1}} = \sqrt{\frac{g^{*2} + 8}{g^{*2}}}. \quad (12)$$

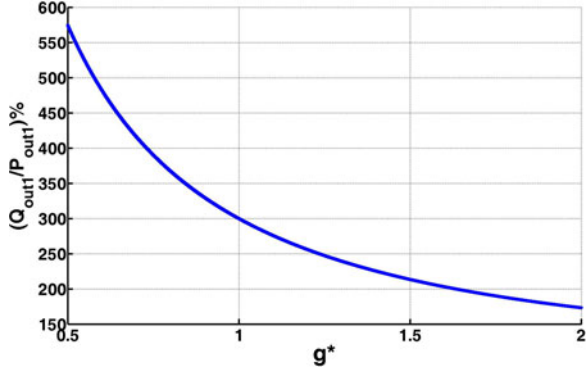


Fig. 8. For Module 1, the ratio of the reactive (circulating) power to the active power for varying peak normalized dc-voltage gain for the DMCI when the inverter is operated using CMS. The DMCI has no circulating-power when it is operated using DMS.

Note that, V_{out} using CMS is a sinusoidal waveform while V_{out1} is a nonsinusoidal waveform. Fig. 8 plots the ratio of Q_{out1} and P_{out1} as a function of the normalized peak dc-voltage gain as captured in (12). The circulating power is significant for lower peak dc-voltage gains leading to additional power loss.

B. Device Rating

Following Fig. 1, the off-state voltage of each device in the DMCI (V_{Qa}, V_{Qb}) is given by the following set of expressions:

$$\begin{cases} V_{Qa} = V_{ca} + \frac{V_{cb}}{n} \\ V_{Qb} = nV_{ca} + V_{cb}. \end{cases} \quad (13)$$

In the steady state, using $V_{ca} = V_{DC}$ and $V_{cb} = V_{out1}$, (13) translates to the following expression:

$$\begin{cases} V_{Qa} = V_{DC} + \frac{V_{out1}}{n} \\ V_{Qb} = nV_{DC} + V_{out1}. \end{cases} \quad (14)$$

The voltage ratings of the devices should be designed for the worst case, which happens at the peak output voltage.

For the DMS-based DMCI, the peak output voltages of Modules 1 and 2 (V_{out1}^* and V_{out2}^*) equal V_{out}^* . However, when DMCI is operated using CMS, the peak output voltage of each module is higher than the V_{out}^* . These can be expressed as follows:

$$\begin{cases} V_{out1}^* = V_{out2}^* = V_{out}^* & \text{for DMS} \\ V_{out1}^* = V_{out}^* + V_{out2}^* (\text{min}) & \text{for CMS} \end{cases} \quad (15)$$

where $V_{out2}^* (\text{min})$ is always positive. Equations (15) and (16) show that the voltage ratings of the devices of the DMCI when operated using CMS are higher than those obtained using DMS. The ratio of the peak voltage of the device using CMS to the peak voltage of the device with DMS can be obtained by substituting (15) into (14). This ratio is rewritten as a function of peak dc-voltage gain using (2) and (3)

$$\frac{V_{Qa}^* (\text{CMS})}{V_{Qa}^* (\text{DMS})} = \frac{V_{Qb}^* (\text{CMS})}{V_{Qb}^* (\text{DMS})} = \frac{V_{DC} + \frac{V_{out1}^*}{n}}{V_{DC} + \frac{V_{out}^*}{n}} \quad (16)$$

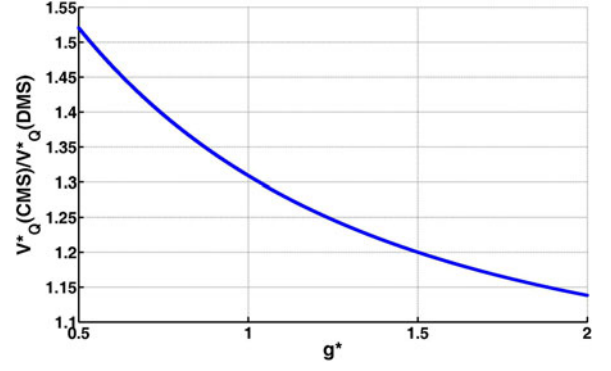


Fig. 9. $V_{Qa}^* (\text{CMS}) / V_{Qa}^* (\text{DMS})$ as a function of g^* .

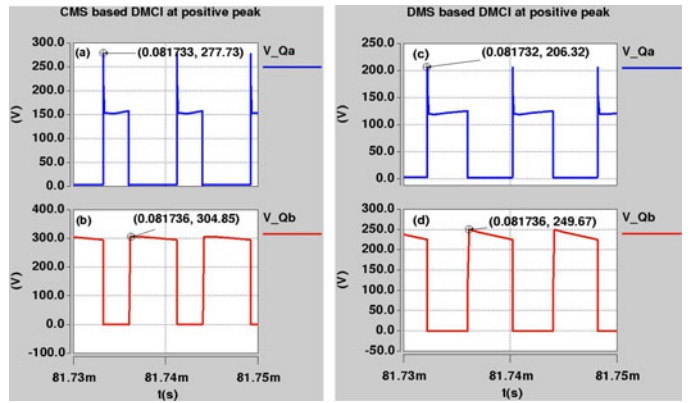


Fig. 10. Simulation results for V_{Qa} and V_{Qb} obtained using CMS and DMS when the output voltage attains maximum positive value.

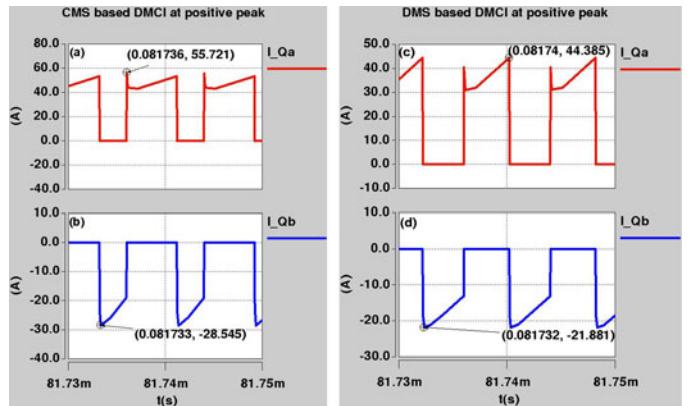


Fig. 11. Simulation results for I_{Qa} and I_{Qb} obtained using CMS and DMS when the output current attains maximum positive value.

where V_{Qa}^* and V_{Qb}^* are peak voltages of the primary side and the secondary side devices, respectively. It is noted that, (16) does not include any device voltage spike, which is dependent on the load, leakage inductance of the transformer, the off-state voltage of the device, and printed-circuit-board layout. As such, the actual peak voltages are slightly higher and (16) indicates an approximate value. Using (2), (8), (9), and (16), the device

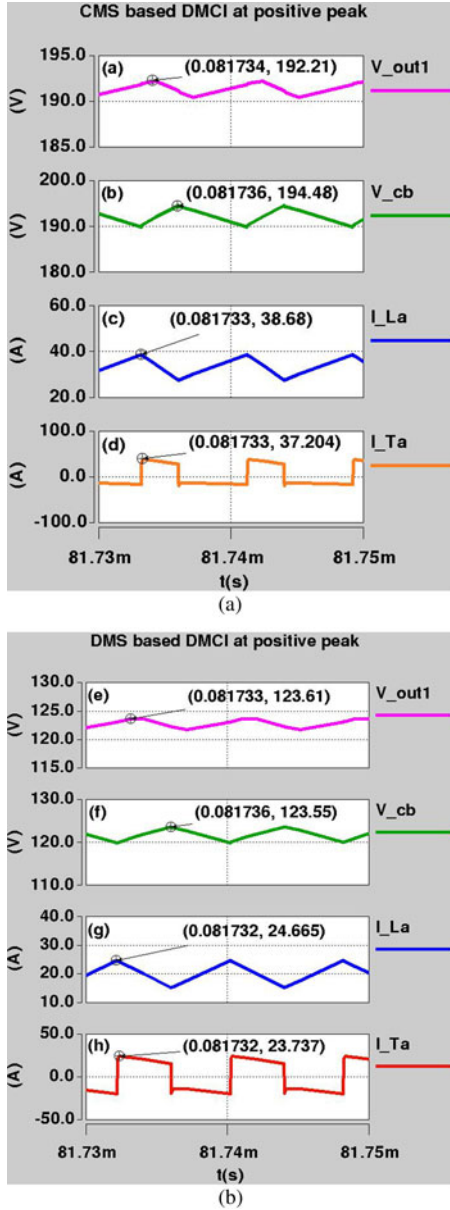


Fig. 12. Simulation results showing V_{out1} , V_{cb} , I_{La} , and I_{Ta} for the DMCI shown in Fig. 1 when the inverter is operated using CMS and DMS and when the output voltage attains maximum positive value.

voltage ratio can be written as a function of g^* as follows:

$$\frac{V_{Q_a}^*(\text{CMS})}{V_{Q_a}^*(\text{DMS})} = \frac{V_{Q_b}^*(\text{CMS})}{V_{Q_b}^*(\text{DMS})} \approx \frac{1 + \frac{g^*}{2} + \sqrt{\left(\frac{g^*}{2}\right)^2 + 1}}{1 + g^*}. \quad (17)$$

The ratio $V_{Q_a}^*(\text{CMS})/V_{Q_a}^*(\text{DMS})$ as described by (17) is plotted in Fig. 9. It is always greater than one and the ratio decreases with increasing normalized dc-voltage gain. The purpose of calculations and plot is to demonstrate the effect of modulation on reduction of device voltage rating, which is modeled well by (17) as shown by simulation and experimental results. However, actual peak voltages of devices also depend on spikes of the switches. The spike on Q_a is due to discharge of the energy stored in the leakage inductance of the transformer and

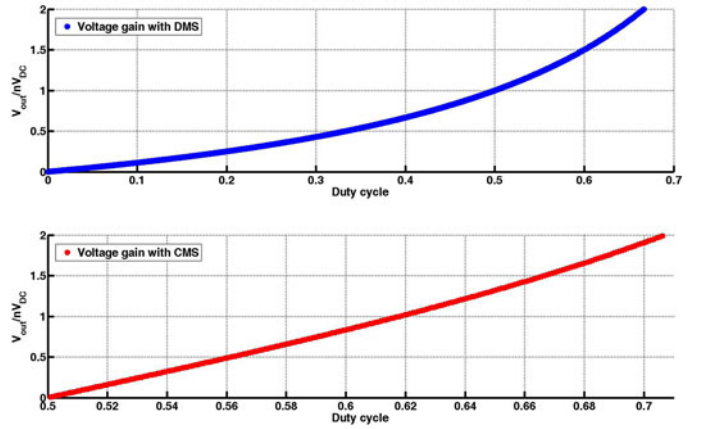


Fig. 13. Normalized dc-voltage gain of the DMCI as a function of the duty cycle when the inverter is operated using DMS and CMS.

parasitic inductances during the turn OFF of Q_a . It mostly depends on the switch turn-off time, snubber circuit, energy stored in leakage inductance of the transformer. The spike on Q_b is due to the reverse recovery of the diode during the diode turn-off.

Fig. 10 shows the (Saber-based) simulation results for the peak drain-to-source voltages of Q_a and Q_b operating with DMS and CMS. These simulations are carried out using circuit parameters that match those of the experimental prototype described in Section IV. Using these parameters, the ratios of $V_{Q_a}(\text{CMS})/V_{Q_a}(\text{DMS})$ and $V_{Q_b}(\text{CMS})/V_{Q_b}(\text{DMS})$ are found to be 1.34 and 1.22, respectively, for $g^* = 1$, $V_{DC} = 60$ V, $V_{out}^* = 120$ V, and an output power (P_{out}) of 500 W. This is found to be close to the theoretically predicted value as shown in Fig. 9 for $g^* = 1$. DMS also reduces the current rating of the devices. This is evident from the simulation results in Fig. 11, which demonstrates the peak-current waveforms for Q_a and Q_b .

In addition, Fig. 12 shows that, using DMS, a reduction in the voltage of output capacitor and blocking capacitor or current ratings of input filter inductor and transformer of the DMCI is also achieved. These simulations are carried out using circuit parameters that match those of the experimental prototype described in Section IV including $g^* = 1$, $V_{DC} = 60$ V, $V_{out}^* = 120$ V, and $P_{out} = 500$ W. Further, all of these results are captured during the positive peak of the output voltage.

C. Distortion

The normalized dc-voltage gain of the DMCI is a nonlinear function of the duty cycle for both CMS and DMS as evident in (2) and (3), respectively. In order to compare the nonlinearity of the two modulation schemes, normalized dc-voltage gains of the DMCI are plotted as a function of the duty cycle in Fig. 13. It shows that the nonlinearity of the normalized dc-voltage gain of the inverter using DMS is more than that obtained using CMS in the given range. The voltage-gain nonlinearity leads to distortion at the output voltage, but it only causes limited number of harmonics at the output voltage. In order to study and compare the nonlinearity effect, the FFT analysis is done for the ideal open-loop output voltage of DMCI operating with CMS and DMS. The results are shown in Figs. 14(a) and (b) at

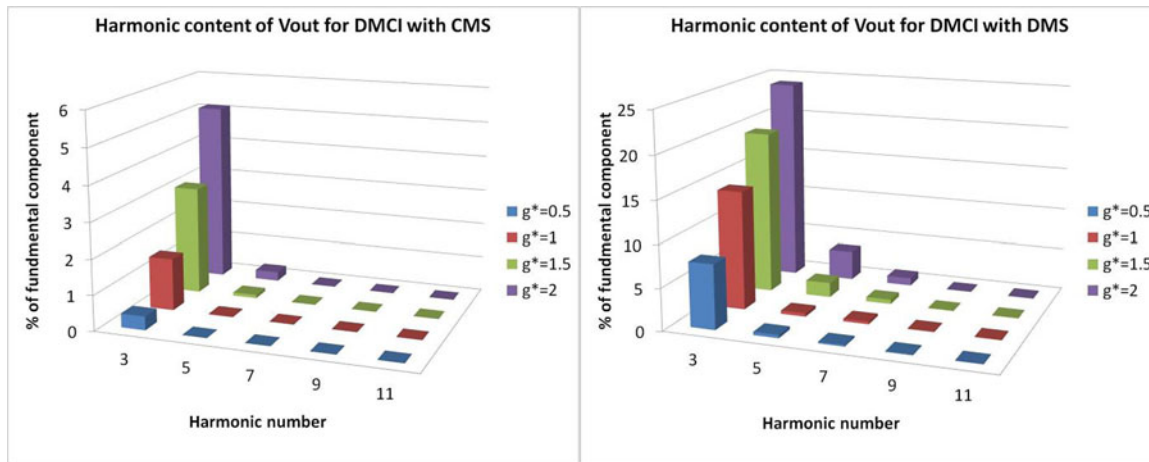


Fig. 14. Harmonic analysis of the output-voltage distortion caused by the nonlinearity in the dc voltage gain of the DMCI operated with (a) CMS and (b) DMS. Magnitudes of the 3rd, 5th, 7th, 9th, and 11th harmonics are shown as a percentage of the magnitude of the fundamental-frequency component of the DMCI output voltage for different peak-voltage gains.



Fig. 15. Experimental prototype of the DMCI. It shows the TMS320F28335 DSP-based digital controller on the top feeding the DMCI power stage at the bottom.

different peak voltage gains for CMS- and DMS-based DMCI, respectively. Comparing the results for CMS and DMS shows that amplitudes of harmonic components of the output voltage of CMS-based DMCI are about 5% at the worst condition, while DMS-based DMCI shows higher harmonic magnitudes. As second conclusion, the magnitude of 11th and higher order harmonics are negligible (less than 0.1%) in practice. Thus, third, fifth, seventh, and ninth harmonics compensators are considered for output voltage distortion problem. It will be demonstrated in Section IV that the nonlinearity effect can be overcome by using a harmonic-compensation of first few harmonics.

IV. EXPERIMENTAL RESULTS

This section provides the experimental results of the DMCI obtained using DMS and CMS. A 500 W experimental prototype of the DMCI, as shown in Fig. 15 is implemented and tested using both modulation schemes. A TMS320F28335 DSP-based digital controller is used for implementing DMS and CMS with closed-loop control, which has 150 MHz clock. Execution time of implemented control loop for CMS-based DMCI takes $1.9 \mu\text{s}$, while this duration for DMS-based controller is about $2.6 \mu\text{s}$. This means roughly 35% more execution time of DMS-

based control for the digital device. Specifications of the DMCI prototype are provided in Table I.

Fig. 16 shows the efficiency of the DMCI for an output voltage of 120 V (RMS) and an output power of 500 W with normalized dc-voltage gain varying between 0.5 and 2 (corresponding to an input-voltage (V_{DC}) variation between 30 V and 120 V). The difference in the efficiencies of the DMCI using DMS and CMS is found to be significant. The improvement is considerably more at lower normalized dc-voltage gain and is consistent with the prediction of Fig. 8.

Next, the peak voltages of the switches (Q_a and Q_c) on the primary side of DMCI obtained using DMS and CMS are measured and plotted in Fig. 17(a). It is noted that, the voltage ratings of the switches on the ac side are proportional to the switches on the dc side with the proportionality constant being the transformer turns ratio. To obtain the plot in Fig. 17, the input voltage is varied between 30 and 120 V for a constant output power of 500 W while keeping the output peak voltage set at 120 V. The results show that the gap between the peak voltage of the switches using DMS and CMS increases (decreases) with decreasing (increasing) normalized dc-voltage gain. The ratios of the measured peak voltages of the primary-side switches of the DMCI are shown in Fig. 17(b) and they are consistent with the predictions in Fig. 9 and the simulation results in Fig. 10.

Next, distortion caused by nonlinearity of the open-loop inverter operating with DMS and CMS is considered. The output voltages of the DMCI operating using DMS and the CMS are shown in Figs. 18(a) and (b), respectively. The peak instantaneous output voltages for both results are set at 170 V (corresponding to 120 V RMS) while the input voltage and output power are set, respectively, at 40 V and 500 W. The DMS yields a THD of 22% for the open-loop DMCI as against a THD of 4% obtained by operating the DMCI using CMS. Further illustration of the problem is provided in Fig. 19 which shows that for the open-loop DMCI, DMS has a progressively adverse effect of the THD of the output voltage with increasing normalized dc-voltage gain. As such, a closed-loop control mechanism to compensate for the harmonic is pursued next.

TABLE I
SPECIFICATIONS OF THE DMCI EXPERIMENTAL PROTOTYPE

Input voltage	Peak output voltage (V_{out}^*)	Output power	Output frequency	Transformer turns ratio (n)	Switching frequency	Primary-side filter inductance	Secondary-side filter inductance
20-120 V	170 V	500 W	60 Hz	2	125 kHz	50 μ H	100 μ H

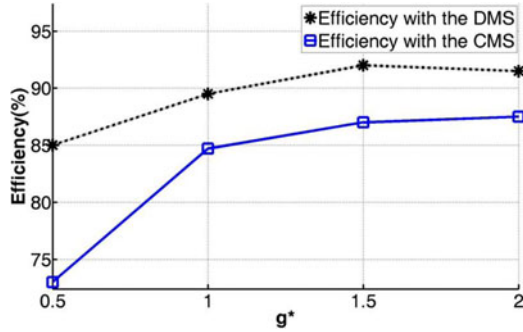


Fig. 16. Experimental efficiency of the DMCI for varying normalized dc peak voltage-gain obtained using DMS and CMS.

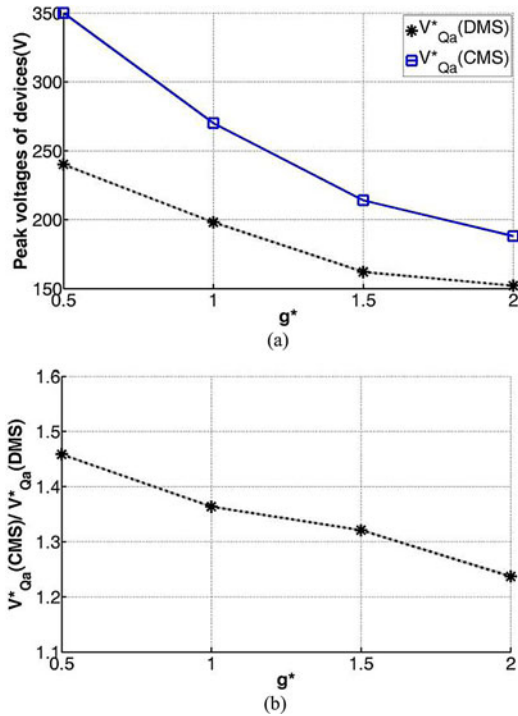


Fig. 17. (a) Experimentally determined peak voltage of the primary-side switches of the DMCI with CMS (solid line) and DMS (dotted line). (b) Ratios of the two traces in (a).

The architecture of the closed-loop controller for the DMCI is shown in Fig. 20. It comprises mechanisms for harmonic compensation. The choice of third, fifth, seventh, and ninth harmonic compensation in Fig. 20 is guided by the determination that when the open-loop DMCI is operated using DMS based on a sinusoidal modulation signal, the resultant output voltage of the inverter is found to have appreciable components of third, fifth, seventh, and ninth harmonics apart from the dominant fundamental 60 Hz ($= \frac{\omega_o}{2\pi}$) component with a desired amplitude of V_{amp} and an initial phase of θ . The choice of the fundamental

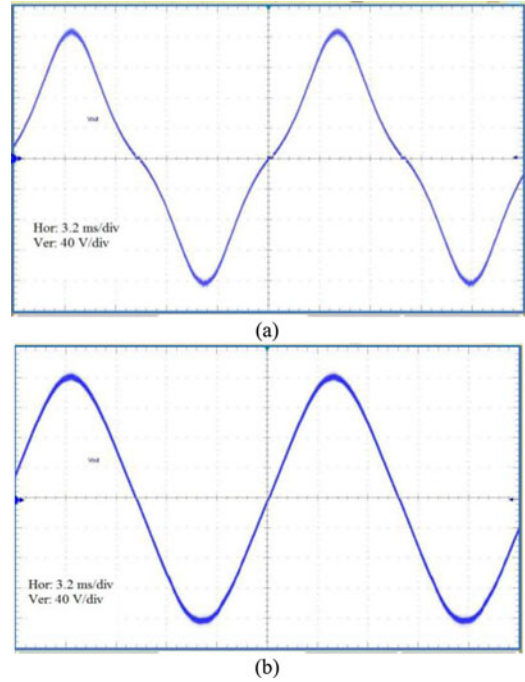


Fig. 18. Experimentally obtained output voltage of the open-loop DMCI operated using (a) DMS (yielding a THD of 22%) and (b) CMS (yielding a THD of 4%). Horizontal scales for both results are set 3.2 ms/div while corresponding vertical scales are set at 40 V/div.

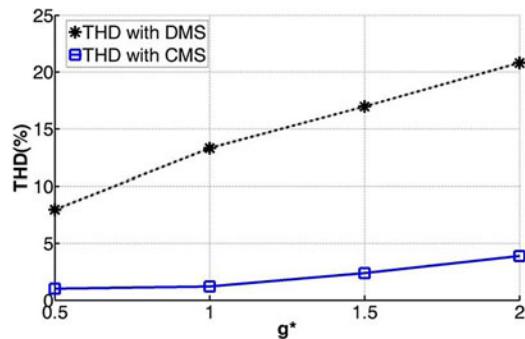


Fig. 19. Experimentally obtained THD of the output voltage of the open-loop DMCI obtained using DMS and CMS as a function of the normalized dc-voltage gain.

and harmonic compensation is based on proportional-resonant (PR) compensating scheme [31] that is tuned to keep a balance between satisfactory steady-state performance and acceptable transient response. The output of the compensation (i.e., comprising fundamental and harmonic compensation) block feeds the control command to the modulator that implements CMS or DMS. The output switching signals of the modulation block are fed to the DMCI. It is noted that, when the DMCI is operated

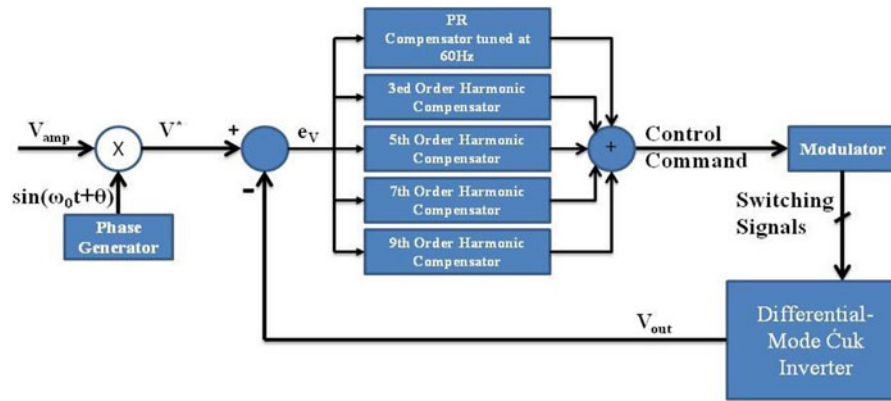


Fig. 20. Architecture of the closed-loop controller for the DMCI.

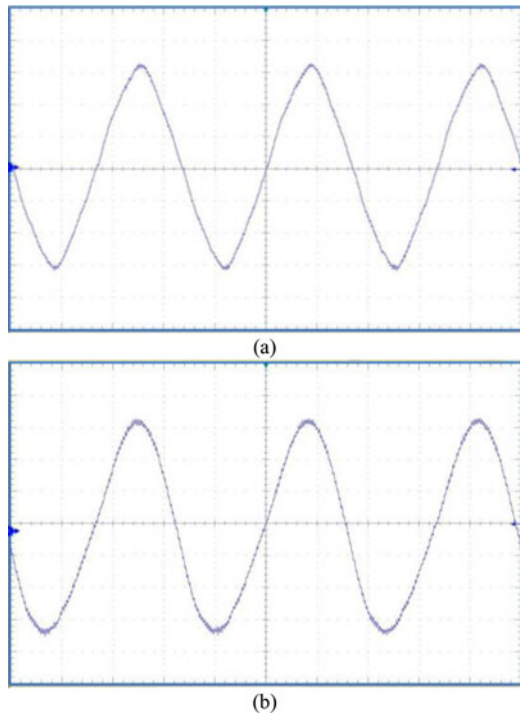


Fig. 21. Experimentally obtained output voltage of the closed-loop DMCI operated using (a) DMS (yielding a THD of 5.5%) and (b) CMS (yielding a THD of 5%). Horizontal scales for both results are set 5 ms/div while corresponding vertical scales are set at 50 V/div.

using CMS, the harmonic compensator is not needed; instead, only a PR-based fundamental-frequency controller is used to close the loop. This is because, and as illustrated in Figs. 13 and 18(b), the DMCI exhibits almost linear characteristics when it is operated using CMS.

The closed-loop output voltages of the DMCI operating using DMS and the CMS are shown in Figs. 21(a) and (b), respectively. The peak instantaneous output voltages for both results are set at 170 V (corresponding to 120 V RMS) while the input voltage and output power are set, respectively, at 40 V and 500 W. The DMS yields a THD of 5.5%, while THD of 5% obtained by operating the DMCI using CMS. Fig. 22 shows the THD of the output voltage of the closed-loop DMCI operated using DMS and CMS. By comparing the open- and closed-loop

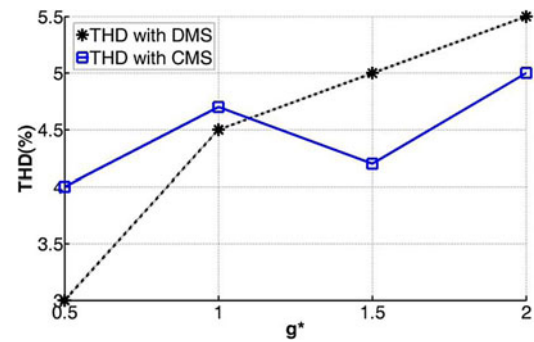


Fig. 22. Experimentally obtained THD of the output voltage of the closed-loop DMCI operated using DMS and CMS as a function of the normalized peak dc-voltage gain of the inverter. It shows a marked improvement in the THD of the closed-loop DMCI using DMS.

results of DMCI shown, respectively, in Figs. 19 and 22, one can observe that the (PR-based) harmonic compensators reduce the THD of the DMS-based closed-loop DMCI. In addition to achieving an acceptable THD, a further goal is to achieve an acceptable transient performance for the DMCI. Consequently, for the DMS-based DMCI, the gains of the fundamental and harmonic compensators have to be so chosen such that an optimal tradeoff between a lower harmonic distortion and a satisfactory transient response is achieved. In our present design, the tuning of the compensator gains are skewed more toward achieving a reduced THD (as evident in Fig. 22) because the open-loop dc-voltage-gain response of the DMS-based DMCI is highly nonlinear, which yields higher distortion. This is further evident in Fig. 23. It shows that even though the topological control of the DMS-based DMCI has to address a reduced-order system (as evident in Fig. 5) as compared to the CMS-based DMCI (as evident in Fig. 2), the transient response of the inverter is slightly slower due to choices of the gains of the PR compensators. Essentially, if the proportional gains of the PR compensators are increased then, while it increases the control bandwidth, it increases distortion because of the spread in the control spectrum around the fundamental and harmonic frequencies. This sets an upper limit on the proportional gains.

In contrast, for the CMS-based closed-loop DMCI, the choice of the PR compensator gain is skewed toward achieving a satisfactory dynamic response. This is because the topological

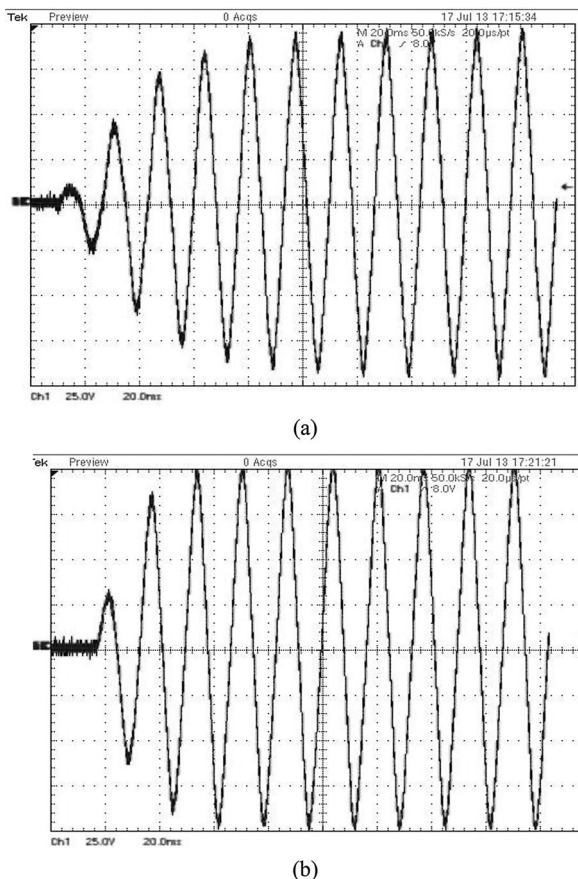


Fig. 23. Transient start-up response of the closed-loop DMCI when it is operated using (a) DMS and (b) CMS. Horizontal and vertical scales for (a) and (b) are set at 20 ms/div and 25 V/div, respectively.

control of the CMS-based DMCI has to address a higher order system as compared to the DMS-based DMCI; and additionally, the open-loop dc-voltage gain of the inverter, as a function of the duty ratio, has a wide range of linearity, which yields reduced THD compared to the DMS-based DMCI. As evident in Fig. 23(b), the transient response of the CMS-based DMCI is better than that obtained using the DMS-based DMCI. However, this improvement in transient response comes at the price of a slight increase in the THD, as evident in Fig. 22. Essentially, while an increase in the proportional gain of the PR compensator increases the control bandwidth, it also spreads the control spectrum around the fundamental harmonic. Even though for the CMS-based open-loop DMCI, the magnitude of the lower order harmonics around the fundamental harmonic is small, the spread in the control spectrum amplifies the response of these lower order harmonics thereby slightly increasing the THD for the closed-loop DMCI.

V. CONCLUSION

The paper describes a DMS for a DMCI and compares the mechanism and performance of the DMS-based DMCI to that of a prior-art CMS-based DMCI. An experimental hardware prototype was developed for the DMCI to validate and compare the results obtained using the two modulation schemes focusing

on energy-conversion efficiency, device rating, output-voltage distortion, and transient response of the inverter. It has been found that DMS, which leads to topological switching of the DMCI, yields significant improvement in efficiency of the inverter compared to that obtained using CMS. This is because DMS eliminates the pathway for circulating reactive power in the DMCI. For the same reason, the reduction in the voltage rating of the DMCI switches is also found to be significant using DMS.

With regard to the THD of the output voltage of the DMCI, CMS demonstrated better results compared to DMS for the inverter when the inverter was operated under open-loop control. The DMS-based DMCI has a better dynamic response because of the reduced order of the topological control system; however, the DMS-based DMCI has a wide range of nonlinearity in its dc-voltage gain, which yields higher THD. Consequently, a closed-loop control for the DMCI-based on harmonic compensation was designed and the experimental results obtained using DMS demonstrated a marked improvement in the THD of the inverter output voltage. The slightly slower response of the DMS-based DMCI is due to the fact that a higher order PR-based harmonic compensation for the closed-loop controller is needed that reduces the control bandwidth. To address this issue, work is currently underway on an optimal controller that promises to address this tradeoff between steady-state and transient performances more effectively.

An overall qualitative comparison between the DMS- and CMS-based operations of the DMCI, as implemented currently, indicates that the DMS-based operation of the DMCI has the potential to yield relatively higher saving in the power stage due to the reduced requirements of the device breakdown-voltage, heat-sinking, and power-handling. However, the DMS-based control scheme, in contrast to the CMS-based control scheme, yields a relatively higher complexity for control implementation.

REFERENCES

- [1] H. S. Kim, M. H. Ryu, J. W. Baek, and J. H. Jung, "High-efficiency isolated bidirectional ac-dc converter for a dc distribution system," *IEEE Trans. Power Electron.*, vol. 28, no. 4, pp. 1642–1654, Apr. 2013.
- [2] S. Harb and R. S. Balog, "Reliability of candidate photovoltaic module-integrated-inverter (PV-MII) topologies—A usage model approach," *IEEE Trans. Power Electron.*, vol. 28, no. 6, pp. 3019–3027, Jun. 2013.
- [3] A. Rahnamaee and S. K. Mazumder, "A soft-switched hybrid-modulation scheme for a dc-link-capacitor-less three-phase pulsating-dc-link inverter," *IEEE Trans. Power Electron.*, vol. 28, no. 8, pp. 3893–3906, Jun. 2014.
- [4] S. K. Mazumder, "A novel hybrid modulation scheme for an isolated high-frequency-link fuel cell inverter," in *Proc. IEEE Power Energy Soc. Gen. Meet.*, 2008, pp. 1–7.
- [5] H. Bayat, J. S. Moghani, S. H. Fathi, and H. Riazmontazer, "Implementation of a 5 level cascade H-bridge inverter using PWM strategy with unequal carrier frequency for optimizing and reducing the switching number," *J. Int. Rev. Elect. Eng.*, vol. 6, no. 1, pp. 23–29, Feb. 2011.
- [6] M. Taheri, J. Milimonfared, H. Bayat, H. Riazmontazer, and H. Noroozi, "Analysis and design of a new soft switching interleaved converter using an integrated transformer," in *Proc. 2nd Power Electron. Drive Syst. Technol.*, Feb. 16–17, 2011, pp. 98–103.
- [7] A. Rahnamaee, J. Milimonfared, and K. Malekian, "Reliability and performance improvement by implementing zero-voltage-switching in high power flyback power supply," *J. Int. Rev. Elect. Eng.*, vol. 4, no. 5, pp. 699–705, Feb. 2009.
- [8] D. Meneses, F. Blaabjerg, O. García, and J.A. Cobos, "Review and comparison of step-up transformerless topologies for photovoltaic ac-module

- application," *IEEE Trans. Power Electron.*, vol. 28, no. 6, pp. 2649–2663, Jun. 2013.
- [9] Z. Zheng, X. Ming, C. Qiaoliang, L. S. Jih, and C. Younghoon, "Derivation, analysis, and implementation of a boost–buck converter-based high-efficiency PV inverter," *IEEE Trans. Power Electron.*, vol. 27, no. 3, pp. 1304–1313, Mar. 2012.
- [10] Z. Honglin, X. Shuai, Y. Geng, and G. Hua, "Modeling and control for a bidirectional buck–boost cascade inverter," *IEEE Trans. Power Electron.*, vol. 27, no. 3, pp. 1401–1413, Mar. 2012.
- [11] Y. Bo, L. Wuhua, G. Yunjie, C. Wenfeng, and H. Xiangning, "Improved transformerless inverter with common-mode leakage current elimination for a photovoltaic grid-connected power system," *IEEE Trans. Power Electron.*, vol. 27, no. 2, pp. 752–762, Feb. 2012.
- [12] J. M. A. Myrzik, "Novel inverter topologies for single-phase stand-alone or grid-connected photovoltaic systems," in *Proc. IEEE 4th Int. Conf. Power Electronic. Drive Syst.*, Oct. 22–25, 2001, pp. 103–108.
- [13] Y. Xue, L. Chang, S. B. Kjaer, J. Bordonau, and T. Shimizu, "Topologies of single-phase inverters for small distributed power generators: an overview," *IEEE Trans. Power Electron.*, vol. 19, no. 5, pp. 1305–1314, Sep. 2004.
- [14] J. M. A. Myrzik and M. Calais, "String and module integrated inverters for single-phase grid connected photovoltaic systems—A review," in *Proc. IEEE Power Tech. Conf.*, vol. 2, Bologna, Italy, Jun. 23–26, 2003, pp. 430–437.
- [15] N. Vazquez, J. Almazan, J. Alvarez, C. Aguiar, and J. Arau, "Analysis and experimental study of buck, boost, and buck-boost inverters," in *Proc. IEEE Power Electron. Spec. Conf.*, 1999, vol. 2, pp. 801–806.
- [16] H. Long, Z. Ming, H. Lijun, Y. Wenxi, and L. Zhengyu, "A family of three-switch three-state single-phase Z-source inverters," *IEEE Trans. Power Electron.*, vol. 28, no. 5, pp. 2317–2329, May 2013.
- [17] T. P. Ching, C. C. Ming, and M. L. Ching, "A novel integrated dc/ac converter with high voltage gain capability for distributed energy resource systems," *IEEE Trans. Power Electron.*, vol. 27, no. 5, pp. 2385–2395, May 2012.
- [18] D. L. Chen and G. L. Wang, "Differential buck dc–dc chopper mode inverters with high-frequency link," *IEEE Trans. Power Electron.*, vol. 26, no. 5, pp. 1444–1451, May 2011.
- [19] R. O. Caceres and I. Barbi, "A boost dc–ac converter; analysis, design, and experimentation," *IEEE Trans. Power Electron.*, vol. 14, no. 1, pp. 134–141, Jan. 1999.
- [20] J. Minsoo, M. Ciobotaru, and V. G. Agelidis, "A single-phase grid-connected fuel cell system based on a boost inverter," *IEEE Trans. Power Electron.*, vol. 28, no. 1, pp. 279–288, Jan. 2013.
- [21] T. Shimizu, K. Wada, and N. Nakamura, "Flyback-type single-phase utility interactive inverter with power pulsation decoupling on the dc input for an ac photovoltaic module system," *IEEE Trans. Power Electron.*, vol. 21, no. 5, pp. 1264–1272, Sep. 2006.
- [22] L. Yanlin and R. Oruganti, "A low cost flyback CCM inverter for ac module application," *IEEE Trans. Power Electron.*, vol. 27, no. 3, pp. 1295–1303, Mar. 2012.
- [23] S. B. Kjaer and F. Blaabjerg, "A novel single-stage inverter for ac-module with reduced low-frequency ripple penetration," in *Proc. 10th Eur. Conf. Power Electron. Appl.*, 2003, pp. 2–4.
- [24] P. Sivasubramanian and S. K. Mazumder, "A differential-mode current-sourced high-frequency-link photovoltaic inverter," in *Proc. IEEE Power Energy Conf. Illinois*, Feb. 2012, pp. 1–9.
- [25] S. Ćuk and R. Erickson, "A conceptually new high-frequency new zero-ripple switching dc-to-dc converter and integrated magnetics," in *Proc. 5th Nat. Solid-State Power Conv. Conf. (Powercon 5)*, May 4–6, 1978, pp. G3.1–G3.22.
- [26] S. K. Mazumder and S. Mehrnami, "A low-device-count single-stage direct-power-conversion solar microinverter for microgrid," in *Proc. IEEE 3rd Int. Symp. Power Electron. Distrib. Gen. Syst.*, Jun. 25–28, 2012, pp. 725–730.
- [27] S. Ćuk, "A new zero-ripple switching dc-to-dc converter and integrated magnetics," *IEEE Trans. Magn.*, vol. M-19, no. 2, pp. 57–75, Mar. 1983.
- [28] S. Mehrnami and S. K. Mazumder, "Modulation scheme of the differential-mode Ćuk inverter for loss mitigation," in *Proc. IEEE Energy Convers. Congr. Expo.*, Sep. 15–19, 2013, pp. 3419–3425.
- [29] J. Knight, S. Shirsavar, and W. Holderbaum, "An improved reliability Ćuk based solar inverter with sliding mode control," *IEEE Trans. Power Electron.*, vol. 21, no. 4, pp. 1107–1115, Jul. 2006.
- [30] V. Valouch, Z. Muller, J. Svec, and J. Tlustý, "Evaluation of IRP, FBD, SD, and generalized non-active power theories," in *Proc. IEEE 27th Conv. Elect. Electron. Eng. Israel*, Nov. 2012, vol. 1, no. 5, pp. 14–17.
- [31] D. N. Zmood and D. G. Holmes, "Stationary frame current regulation of PWM inverters with zero steady state error," in *Proc. IEEE 34th Annu. Power Electron. Spec. Conf.*, 1999, vol. 2, pp. 1185–1190.



Siamak Mehrnami (S'11) received the B.S. degree in electrical engineering from the University of Tabriz, Iran, in 2006, and the M.S. degree in electrical engineering from the University of Tehran, Iran, in 2009. He is currently working toward the Ph.D. degree in electrical engineering at the University of Illinois at Chicago, USA.

He was a Contractor and a member of solar car team of the University of Tehran from 2009 to 2011. He was also Design Engineer at renewable energy organization of Iran from 2010 to 2011. Since 2011, he has been a Research Assistant at the Laboratory of Energy and Switching Electronics Systems at the University of Illinois at Chicago. His research area includes but not limited to high frequency link inverters, power electronics applications in renewable energy, motor driver, electrical vehicle and smart grid. He has published two Journal papers and six IEEE conferences.

Mr. Mehrnami received third best paper award in PEDG 2013 conference.



Sudip K. Mazumder (S'97–M'01–SM'03) received the Ph.D. degree from the Department of Electrical and Computer Engineering of Virginia Tech, VA, USA, in 2001.

He is the Director of the Laboratory for Energy and Switching-Electronics Systems and a Professor in the Department of Electrical and Computer Engineering at the University of Illinois, Chicago (UIC). He has more than 22 years of professional experience and has held R&D and design positions in leading industrial organizations and has served as a Technical Consultant for several industries. He also serves as the President of NextWatt LLC, a small business organization that he setup in 2008. His research interests include 1) interactive power-electronics/power networks, smart grid, and energy storage; 2) renewable and alternative energy-based power electronics systems for distributed generation and microgrid; and 3) optically triggered wide-bandgap power-electronics device and control technologies and SiC and GaN device-based high-frequency, high-temperature, and high-voltage power electronics.

Dr. Mazumder has been awarded about 40 sponsored projects by NSF, DOE, ONR, ARPA-E, CEC, EPA, AFRL, NASA, NAVSEA, and multiple leading industries in aforementioned areas, since joining the UIC in 2001. He has published more than 160 refereed papers in prestigious journals and conferences and has published one book and eight book chapters. About 50% of his journal papers are published in IEEE transactions with a current impact factor above 4. He has presented 53 invited/plenary/keynote presentations at leading organizations and institutions and currently, he also holds seven issued and three pending patents. He received in 2013, the prestigious University Scholar Award from the University of Illinois and in 2011, the Teaching Recognition Program Award at the UIC. In 2008 and 2006, he received the prestigious Faculty Research Award from the UIC for outstanding research performance and excellent scholarly activities. He also received the ONR Young Investigator Award and the NSF CAREER Awards, in 2005 and 2003, respectively, and IEEE Prize Paper Awards, in 2002, 2007, and 2013, respectively, and the IEEE International Future Energy Challenge Award in 2005. He served as the first Editor-in-Chief for the *International Journal of Power Management Electronics* (currently known as *Advances in Power Electronics*) between 2006 and 2009. Currently, he serves as the Guest-Editor-in-Chief for the IEEE TRANSACTIONS ON POWER ELECTRONICS SPECIAL ISSUE ON HIGH-FREQUENCY-LINK POWER-CONVERSION SYSTEMS (2013–2014) and the Guest Editor for the IEEE TRANSACTIONS ON INDUSTRIAL ELECTRONICS SPECIAL SECTION ON CONTROL STRATEGIES FOR SPATIALLY DISTRIBUTED INTERACTIVE POWER NETWORKS (2013–2014). Currently, he also serves as an Associate Editor for the IEEE TRANSACTIONS ON INDUSTRIAL INFORMATICS (since 2014), the IEEE TRANSACTIONS ON POWER ELECTRONICS (since 2009), the IEEE TRANSACTIONS ON INDUSTRIAL ELECTRONICS (since

2003), and the IEEE TRANSACTIONS ON AEROSPACE AND ELECTRONICS SYSTEMS (since 2008). He is also an Editorial Board Member for Advances in Power Electronics. Previously, he has also served as an Associate Editor for the IEEE TRANSACTIONS ON CIRCUITS AND SYSTEMS and the IEEE POWER ELECTRONICS LETTER. He has also served as the Guest Coeditor for the following Transaction Special Issues: IEEE TRANSACTIONS ON POWER ELECTRONICS SPECIAL ISSUE ON POWER ELECTRONICS IN DC DISTRIBUTION SYSTEMS (2011–2013) and ADVANCES IN POWER ELECTRONICS SPECIAL ISSUE ON ADVANCES IN POWER ELECTRONICS FOR RENEWABLE ENERGY (2010–2011). He is currently serving as a Plenary Chair for the 2015 IEEE Energy Conversion Congress and Exposition. He is also serving as the Technical Awards Committee Chair for the IEEE Power Electronics Society (PELS) Technical Committee on Sustainable Energy Systems (SES). He is also serving as a Chair for the IEEE PELS Subcommittee on Distributed Generation and Renewable Energy and for IEEE PELS Subcommittee on Power Semiconductors, and Member for IEEE PELS Standards Subcommittee and IEEE IES Network Control Systems and IEEE IES Power Electronics Technical Committees. In 2010, he served as the Chair, Student/Industry Coordination Activities for IEEE Energy Conversion Congress and Exposition, which is the largest conference in power electronics today in North America. He serves/served as a Steering Committee Member for 2014 Power Electronics and Application Conference and Exposition and as an Advisory Committee Member for 2012 IEEE India International Conference on Power Electronics as well as for 2010 IEEE International Symposium on Power Electronics for Distributed Generation Systems. He also served as the Cochair for SES. In addition, he is serving/has served as Technical Program Committee

Member for numerous IEEE sponsored and other reputed conferences including IEEE Energy Conversion Congress and Exposition, IEEE Applied Power Electronics Conference and Exposition, IEEE Industrial Electronics Conference, IEEE International Symposium on Power Electronics for Distributed Generation Systems. He was one of the five leading researchers invited by the inaugural 2012 Clean Energy Trust Show Case, an event that connects entrepreneurs, investors and researchers who can work together to commercialize the latest clean technology, to deliver his vision on Smart Grid. Between 2010 and 2011, he also served as an Advisory Council Member for Vice Chancellor for Research's Urban Resilience and Global Environment at the UIC. In 2009 and 2010, he also served as the Expert Representative on Smart Grid for the UIC at the Midwestern Great Lakes Alliance for Sustainable Energy Research (GLASER) initiative. In 2008, he was invited by DOE to participate along with several leading industries and selected academic professionals regarding High MW Power Converter for next generation power grid. In 2008, he was invited by NSF to participate in a unique workshop (comprising leading industries and research experts) leading to decision on nation's specific R&D focus on energy and energy distribution over the next 10 and 50 years. He has also been invited to serve as the Working Group Committee Member for IEEE P1676, which focuses on Control Architecture for High Power Electronics (> 1 MW) used in Electric Power Transmission and Distribution Systems. In 2009, he was also part of the team that wrote the NSF and National Coordination Office for Networking and Information Report on Research Directions for Future Cyber-Physical Energy Systems. He has also served as a panel reviewer and reviewer for NSF, DOE, ARPA-E, CRDF, and AAAS.